



A discrete dislocation analysis of bending

H.H.M. Cleveringa^{a,*}, E. Van der Giessen^a, A. Needleman^b

^a*Delft University of Technology, Koiter Institute Delft, Mekelweg 2, 2628 CD Delft, The Netherlands*

^b*Brown University, Division of Engineering, Providence, RI 02912, USA*

Received in revised form 28 January 1999; accepted 28 January 1999

Abstract

Bending of a strip in plane strain is analyzed using discrete dislocation plasticity where the dislocations are modeled as line defects in a linear elastic medium. At each stage of loading, superposition is used to represent the solution in terms of the infinite medium solution for the discrete dislocations and a complementary solution that enforces the boundary conditions, which is non-singular and obtained from a linear elastic, finite element solution. The lattice resistance to dislocation motion, dislocation nucleation and dislocation annihilation are incorporated into the formulation through a set of constitutive rules. Solutions for cases with multiple slip systems and with a single slip system are presented. The bending moment versus rotation relation and the evolution of the dislocation structure are outcomes of the boundary value problem solution. The effects of slip geometry, obstacles to dislocation motion and specimen size on the moment versus rotation response are considered. Also, the evolution of the dislocation structure is studied with emphasis on the role of geometrically necessary dislocations. The dislocation structure that develops leads to well-defined slip bands, with the slip band spacing scaling with the specimen height. © 1999 Published by Elsevier Science Ltd. All rights reserved.

Keywords: A. Dislocations; Bending

1. Introduction

In classical elasticity theory, pure bending of a strip gives rise to a linear normal stress distribution, with the inner and outer fibers having the maximum stress magnitude, but opposite sign. For an elastic–plastic solid, yielding begins simultaneously at the inner and outer fibers (assuming equal flow strengths in tension and compression) and the plastic zone propagates towards the centerline as deformation proceeds. Even if the material is ideally plastic, the bending moment increases until it attains a value 1.5 times that required for initial yield, at which point plastic collapse ensues.

* Corresponding author.

The situation is not so simple for bending of a single crystal. Even in the elastic range, the anisotropic elastic properties affect the stress distribution. For single crystals of structural metals, e.g. Al and Fe, the plastic anisotropy that comes from the limited number of slip systems is more significant. Within the context of continuum slip theory, (e.g. Peirce et al., 1983), the dependence of the response on the orientation of the crystal axes with respect to the axis of bending can be accounted for. However, the continuum slip framework ignores the discreteness of dislocations. One of the notable discrete dislocation effects is that dislocation generation and motion in plastic bending of a single crystal is not a purely stochastic process but requires a density of geometrically necessary dislocations, (Nye, 1953; Ashby, 1970). In addition, the stress and strain distributions within a bent dislocated crystal can be quite different from what continuum plasticity predicts. These effects should be expected to be significant during plastic deformation of micron-sized structural elements in, for example, micromachines that carry bending loads.

In this paper, we carry out full boundary value problem solutions for bending of a plane strain strip, where plastic flow arises from the collective motion of large numbers of dislocations. The formulation is that of Van der Giessen and Needleman (1995) as applied by Cleveringa et al. (1997), but here generalized to account for multiple slip systems. Attention is restricted to small strains with the dislocations modeled as line defects in an isotropic linear elastic solid. The stresses and strains are written as superpositions of fields due to the discrete dislocations, which are singular inside the body, and complementary (image) fields that enforce the boundary conditions. This leads to a linear elastic boundary value problem for the smooth complementary fields which is solved by the finite element method. Thus, the long range interactions between dislocations are accounted for through the continuum elasticity fields. Drag during dislocation motion, interactions with obstacles, and dislocation nucleation and annihilation are also accounted for. These are not represented by the elasticity description of dislocations and are incorporated into the formulation through a set of constitutive rules which are based on those proposed by Kubin et al. (1992).

The focus of analyses of discrete dislocation plasticity, (e.g. Amodeo and Ghoniem, 1990; Fang and Dahl, 1993; Groma and Pawley, 1993; Bréchet et al., 1996; Zbib et al., 1998) has generally been on stress-strain relations and/or the emergence of organized dislocation structures. Fewer studies have addressed boundary value problems. Recently, Polonsky and Keer (1996), Fivel et al. (1996) and Zacharopoulos et al. (1997) have presented particular boundary value problem solutions for dislocated solids using various methods to obtain image fields for large numbers of dislocations. An advantage of the finite element method used in Van der Giessen and Needleman (1995), Cleveringa et al. (1997) and here is its adaptability to rather general boundary value problems.

It is emphasized that in the analyses to be presented here, the plastic stress-strain response and the evolution of the dislocation structure are outcomes of the boundary value problem solution. By way of contrast, in a continuum formulation the plastic stress-strain response is an input, whereas conventional dislocation analyses typically postulate a dislocation structure (e.g. Nye, 1953; Ashby, 1970; Evans, 1995).

2. Problem formulation

The formulation in Van der Giessen and Needleman (1995) and Cleveringa et al. (1997) is briefly described. The computation of the deformation history is carried out in an incremental manner. At a given time t the position of each dislocation in the body is known and the body is in equilibrium with the applied loads and displacements. An increment of loading is applied. Both the equilibrium stress field and the dislocation structure at $t + \Delta t$ need to be determined.

Each time step involves three main computational stages: (i) determining the forces on the dislocations, i.e. the Peach–Koehler force; (ii) determining the rate of change of the dislocation structure, which involves the motion of dislocations, the generation of new dislocations, their mutual annihilation, and their possible pinning at obstacles; and (iii) determining the stress and strain state for the updated dislocation arrangement.

The method for determining the current state of the body V with the current dislocation distribution is an extension of the formulation of Lubarda et al. (1993). The key idea is illustrated in Fig. 1. The displacement, strain and stress fields are written as the superposition of two fields,

$$\mathbf{u} = \tilde{\mathbf{u}} + \hat{\mathbf{u}}, \quad \boldsymbol{\epsilon} = \tilde{\boldsymbol{\epsilon}} + \hat{\boldsymbol{\epsilon}}, \quad \boldsymbol{\sigma} = \tilde{\boldsymbol{\sigma}} + \hat{\boldsymbol{\sigma}} \quad \text{in } V, \quad (1)$$

respectively. The (\sim) fields are the superposition of the fields of the individual dislocations, in their current configuration, but in an infinite medium of the homogeneous matrix material, and are obtained by superposition of the fields ($\mathbf{u}^i, \boldsymbol{\epsilon}^i, \boldsymbol{\sigma}^i$) associated with the individual dislocations,

$$\tilde{\mathbf{u}} = \sum_i \mathbf{u}^i, \quad \tilde{\boldsymbol{\epsilon}} = \sum_i \boldsymbol{\epsilon}^i, \quad \tilde{\boldsymbol{\sigma}} = \sum_i \boldsymbol{\sigma}^i \quad (i = 1, \dots, n) \quad (2)$$

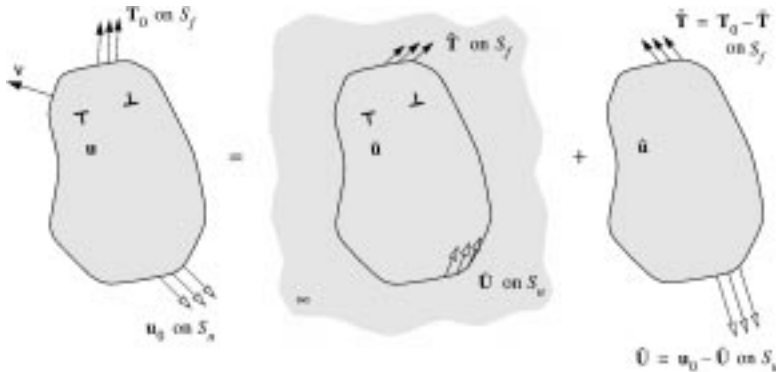


Fig. 1. (a) Definition of the boundary value problem for a dislocated body with elastic inclusions; (b) decomposition into the problem of interacting dislocations in the homogeneous infinite solid (\sim fields) and the complementary problem for the nonhomogeneous body without dislocations (\wedge fields).

where n is the number of dislocations in the current configuration. The (\sim) fields give rise to tractions $\tilde{\mathbf{T}}$ and displacements $\tilde{\mathbf{U}}$ on the boundary of the body.

The $(\hat{})$ fields represent the image fields that correct for the actual boundary conditions on S . The governing equations for the $(\hat{})$ fields are

$$\left. \begin{aligned} \nabla \cdot \hat{\boldsymbol{\sigma}} &= 0 \\ \hat{\boldsymbol{\epsilon}} &= \text{sym}(\nabla \otimes \hat{\mathbf{u}}) \end{aligned} \right\} \text{ in } V \quad (3)$$

$$\hat{\boldsymbol{\sigma}} = \mathcal{L} : \hat{\boldsymbol{\epsilon}} \quad (4)$$

$$\left. \begin{aligned} \boldsymbol{\nu} \cdot \hat{\boldsymbol{\sigma}} &= \hat{\mathbf{T}} = \mathbf{T}_0 - \tilde{\mathbf{T}} & \text{on } S_f \\ \hat{\mathbf{u}} &= \mathbf{U}_0 - \tilde{\mathbf{U}} & \text{on } S_u \end{aligned} \right\} \quad (5)$$

Here, ‘sym’ denotes the symmetric part of a tensor, S_f is the portion of the boundary on which tractions are prescribed, S_u is the portion of the boundary on which displacements are prescribed, \mathbf{T}_0 and \mathbf{U}_0 are the prescribed traction and displacement vectors, respectively, and $\boldsymbol{\nu}$ is the outer unit normal to S_f . A key point is that the $(\hat{})$ fields are smooth, so that Eqs. (3)–(5) constitute a conventional linear elastic boundary value problem that can be conveniently solved by the finite element method.

The elastic properties are taken to be isotropic, for convenience, and the moduli \mathcal{L} in Eq. (4) are written in the form

$$\mathcal{L} = \frac{E}{1+\nu} \left[\mathbf{I}' + \frac{\nu}{1-2\nu} \mathbf{I} \otimes \mathbf{I} \right] \quad (6)$$

where E is Young’s modulus, ν is Poisson’s ratio, and \mathbf{I} and \mathbf{I}' are the second and fourth order identity tensors, respectively. We take $E = 70$ GPa and $\nu = 0.33$.

Here, this generally three-dimensional methodology is applied in two dimensions with straight edge dislocations on multiple, possibly intersecting slip planes. The dislocation fields in an infinite medium can be found in standard texts, such as (Nabarro, 1967; Hirth and Lothe, 1968). Assuming dislocation glide only, the variation of the potential energy of the body due to infinitesimal variations of the position of the i th dislocation is governed by the Peach–Koehler force f^i given by

$$f^i = \mathbf{n}^i \cdot \left(\hat{\boldsymbol{\sigma}} + \sum_{j \neq i} \boldsymbol{\sigma}^j \right) \cdot \mathbf{b}^i \quad (7)$$

with \mathbf{n}^i the slip plane normal and the Burgers vector \mathbf{b}^i of dislocation i . The direction of this force is in the slip plane and normal to the dislocation line. It is this force that will determine the evolution of the dislocation, as will be discussed subsequently.

The Peach–Koehler force includes the interactions with all other dislocations in the material. The summation in Eq. (7) is carried out in a straightforward, exact manner; the number of dislocations in the simulations to be presented are low enough so that the use of fast multipole expansions (Wang and LeSar, 1995; Rodin, 1998) is not yet advantageous.

The magnitude of the glide velocity v^i of dislocation i is taken to be linearly related to the Peach–Koehler force through the drag relation

$$f^i = Bv^i \quad (8)$$

where B is the drag coefficient. The value of B is taken as $B = 10^{-4}$ Pa s, which is a representative value for aluminium, Kubin et al. (1992). Dislocation climb is not considered. Inside dislocation pile-ups, the position of dislocations is quite unstable, which leads to high velocity oscillatory motions. In order to reduce the computational burden of following these essentially irrelevant vibrations, we apply a velocity cut-off. For the material parameters used here, a cut-off velocity of 20 m/s has been found to be low enough to be effective and high enough not to affect the results significantly. Another change in the algorithm compared to previous work (Cleveringa et al., 1997), is that we no longer use an adaptive time stepping scheme but a fixed time step of $\Delta t = 5 \times 10^{-10}$ s. As a consequence, individual events of dipole generation or annihilation may be timed slightly incorrectly, but the overall results are not significantly affected for the present parameter values. The number of incremental steps to a given amount of strain is, however, typically reduced by 2 orders of magnitude compared with the time stepping scheme in (Cleveringa et al., 1997).

New dislocation pairs are generated by simulating Frank–Read sources. The initial dislocation segment of a Frank–Read source bows out until it produces a new dislocation loop and a replica of itself. The Frank–Read source is modeled in terms of a critical value of the Peach–Koehler force, the time it takes to generate a dislocation loop and the size of the generated loop. In two dimensions, this is simulated by point sources which generate a dislocation dipole when the magnitude of the Peach–Koehler force at the source exceeds a critical value $\tau_{\text{nuc}}b$ during a period of time t_{nuc} . The distance L_{nuc} between the dislocations is taken to be specified by

$$L_{\text{nuc}} = \frac{E}{4\pi(1 - \nu^2)} \frac{b}{\tau_{\text{nuc}}}. \quad (9)$$

At this distance, the shear stress of one dislocation acting on the other is balanced by the slip plane shear stress. The strength of the dislocation sources is randomly chosen from a Gaussian distribution with mean strength $\bar{\tau}_{\text{nuc}} = 50$ MPa and standard deviation of $0.2\bar{\tau}_{\text{nuc}}$. From Eq. (9), the mean nucleation distance is $L_{\text{nuc}} = 125.0 b$ and b is specified to have the value 0.25 nm. The nucleation time for all sources is taken as $\tau_{\text{nuc}} = 0.01 \mu\text{s}$.

Annihilation of two dislocations with opposite Burgers vector occurs when they are sufficiently close together. This is modeled by eliminating two dislocations when

they are within a material-dependent, critical annihilation distance L_e , which is specified as $L_e = 6b$ (Kubin et al., 1992).

In some calculations, obstacles to dislocation motion are included that are modeled as fixed points on a slip plane. Such obstacles account for the effects of small precipitates or for dislocations on other slip systems in blocking slip. Pinned dislocations can only pass the obstacles when their Peach–Koehler force exceeds an obstacle dependent value $\tau_{\text{obs}}b$. When present, the obstacles are all taken to have the same strength $\tau_{\text{obs}} = 150 \text{ MPa}$.

The boundary value problem addressed is sketched in Fig. 2. A plane strain strip of dimension $L \times h$ is subject to a prescribed rotation along its edges. With the x_1 – x_2 -plane being the plane of deformation, the boundary conditions are

$$u_1 = \pm(\theta x_2 + U), \quad \sigma_{12} = 0 \quad \text{on } x_1 = \pm \frac{L}{2} \quad (10)$$

$$\sigma_{12} = 0, \quad \sigma_{22} = 0 \quad \text{on } x_2 = \pm \frac{h}{2} \quad (11)$$

where the imposed rotation is θ . The work-conjugate bending moment, M , is given by

$$M = \int_{-h/2}^{h/2} x_2 \sigma_{11}(\pm L/2, x_2) dx_2 \quad (12)$$

In the elastic regime, σ_{11} is linear in x_2 and other in-plane stress components vanish. Also, the curvature k is uniform and equal to $2\theta/L$, while the quantity U in Eq. (10) vanishes.

As soon as dislocations are present, U no longer vanishes. Then, U is determined from the condition that the tensile force on the strip vanishes, i.e.

$$\int_{-h/2}^{h/2} \sigma_{11}(\pm L/2, x_2) dx_2 = 0 \quad (13)$$

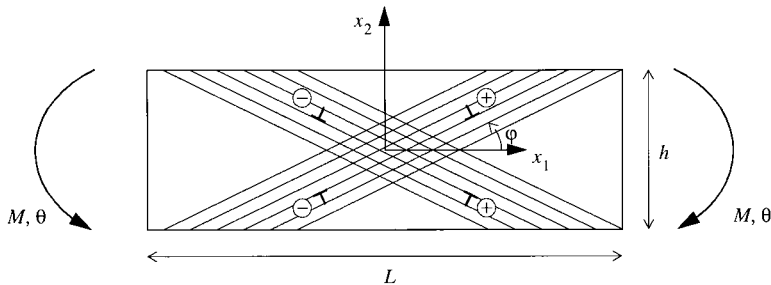


Fig. 2. Sketch of the boundary value problem.

With the decomposition Eq. (1), the condition Eq. (13) can be written as

$$\int_{-h/2}^{h/2} \hat{\sigma}_{11}(\pm L/2, x_2) dx_2 = - \int_{-h/2}^{h/2} \tilde{\sigma}_{11}(\pm L/2, x_2) dx_2 \quad (14)$$

for the $(\hat{\cdot})$ fields, given the $(\tilde{\cdot})$ fields of the dislocations. The value of U is obtained by writing the $(\hat{\cdot})$ fields as a linear superposition of two fields:

1. The field $(\hat{\cdot})^{(1)}$ that satisfies the boundary conditions

$$\hat{\sigma}_{11}^{(1)} = -\tilde{\sigma}_{11}, \quad \hat{\sigma}_{12}^{(1)} = -\tilde{\sigma}_{12} \quad \text{on } x_2 = \pm \frac{h}{2}; \quad (15)$$

$$\hat{u}_1^{(1)} = -\tilde{u}_1 \pm \theta x_2, \quad \hat{\sigma}_{12}^{(1)} = -\tilde{\sigma}_{12} \quad \text{on } x_1 = \pm \frac{L}{2}. \quad (16)$$

Hence, this field corrects for the boundary tractions and displacements caused by the dislocations and incorporates the prescribed rotation.

2. The $(\hat{\cdot})^{(2)}$ field corresponding to uniaxial straining with an arbitrary (e.g. unit) end displacement U_0 , i.e.

$$\hat{\sigma}_{11}^{(2)} = 0, \quad \hat{\sigma}_{12}^{(2)} = 0 \quad \text{on } x_2 = \pm \frac{h}{2}; \quad (17)$$

$$\hat{u}_1^{(2)} = \pm U_0, \quad \hat{\sigma}_{12}^{(2)} = 0 \quad \text{on } x_1 = \pm \frac{L}{2}, \quad (18)$$

independent of the dislocation fields.

Making use of the linearity of the problem, the complete solution for the displacement field, \hat{u}_i , is written as

$$\hat{u}_i = \hat{u}_i^{(1)} + \lambda \hat{u}_i^{(2)}. \quad (19)$$

With $U = \lambda U_0$, it follows from Eqs. (15)–(18) that this field satisfies the boundary conditions Eqs. (10) and (11). The factor λ is determined so that the condition Eq. (14) for vanishing axial force is satisfied:

$$\lambda = - \frac{\int_{-h/2}^{h/2} \left(\hat{\sigma}_{11}^{(1)}(\pm L/2, x_2) + \tilde{\sigma}_{11}(\pm L/2, x_2) \right) dx_2}{\int_{-h/2}^{h/2} \hat{\sigma}_{11}^{(2)}(\pm L/2, x_2) dx_2}. \quad (20)$$

The scaling factor λ is calculated separately for $x_1 = L/2$ and $x_1 - L/2$. Because of numerical errors, these respective values need not be identical, but they were found to be the same to within three significant digits for all cases presented.

The calculations are carried out using a finite element discretization of the governing Eqs. (3) and (4) for the ($\hat{\cdot}$) fields. Here, four-node rectangular elements are used that are based on a mixed Hellinger–Reissner variational principle. In addition to the standard bilinear interpolation for the displacement field, this formulation assumes independent interpolations for the stress components. Linear variations of the normal stresses $\hat{\sigma}_{11}$ and $\hat{\sigma}_{22}$ are assumed in the x_2 and x_1 directions, respectively, while the shear stress $\hat{\sigma}_{12}$ is taken to be constant within each element, thus totalling 5 stress parameters (i.e. 8 degrees of freedom minus three rigid body motions). Integrations of the functional over each element can be readily performed in closed form. These elements have been known for a long time to give an accurate description of the stress gradients in bending (Besseling, 1965). Prior to the computation of the dislocation interactions, the element stresses are averaged over the nodes in order to obtain a continuous $\hat{\sigma}_{ij}$ field over the mesh.

3. Numerical results

3.1. Reference case

Most calculations are carried out for a strip having dimensions $L = 12 \mu\text{m}$ and $h = 4 \mu\text{m}$ (see Fig. 2) subjected to a bending rate of $\dot{\theta} = 0.5 \times 10^3 \text{ s}^{-1}$. The 90×30 quadrilateral mesh used in the computations for this strip is shown in Fig. 3(a) while the contours of σ_{11} in Fig. 3(b) show that the finite element formulation used can reproduce the bending stress distribution in the elastic range without end effects. The computed bending moment agrees with the exact value to within 0.1%.

The curve of moment versus imposed rotation is shown in Fig. 4 for a case where there are three slip systems, oriented at $\varphi = \pm 30^\circ$ from the x_1 -axis (see Fig. 2) and parallel to the x_2 -axis ($\varphi = +90^\circ$). The $\pm 30^\circ$ slip planes are distributed such that none intersects with the left- or right-hand faces, where the displacements are prescribed, in order to avoid numerical complications when dislocations would exit the material through these edges. The 90° slip planes are introduced only over the central zone of width $L - h/\tan 30^\circ$ where the $\pm 30^\circ$ slip planes intersect. With a slip plane spacing of 100 Burgers vectors, a total of 404 slip planes results. The material is taken to be initially dislocation-free and obstacle-free, while 808 dislocation sources are distributed evenly over the three slip systems. In Fig. 4, and subsequently, the moment M is normalized by a reference moment, M_{ref} , defined by

$$M_{\text{ref}} = \frac{2}{h} \int_{-h/2}^{h/2} \bar{\tau}_{\text{nuc}} x_2^2 dx_2 = \frac{2}{3} \bar{\tau}_{\text{nuc}} \left(\frac{h}{2} \right)^2 \quad (21)$$

The reference moment is the moment that would result from a linear stress distribution $\bar{\tau}_{\text{nuc}} x_2 / (h/2)$.

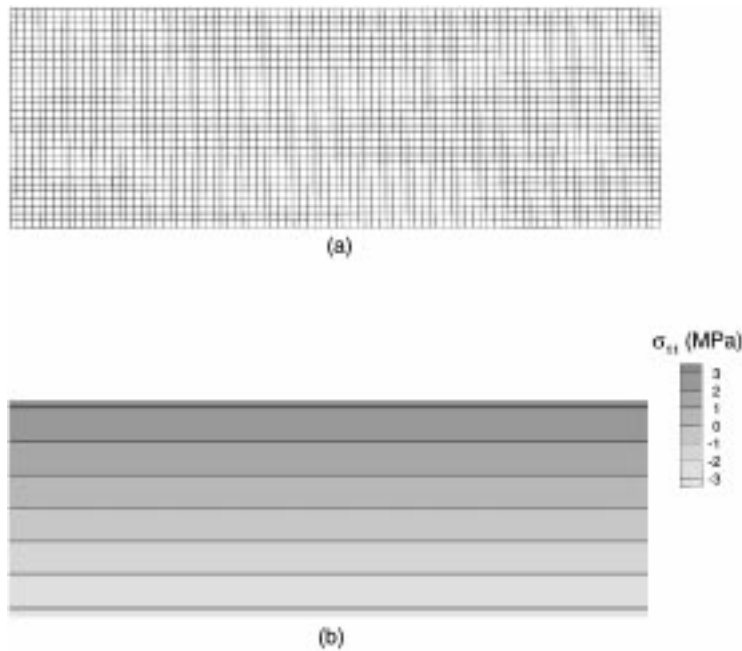


Fig. 3. (a) The 90×30 quadrilateral mesh used in the computations; (b) contours of σ_{11} in the elastic range.

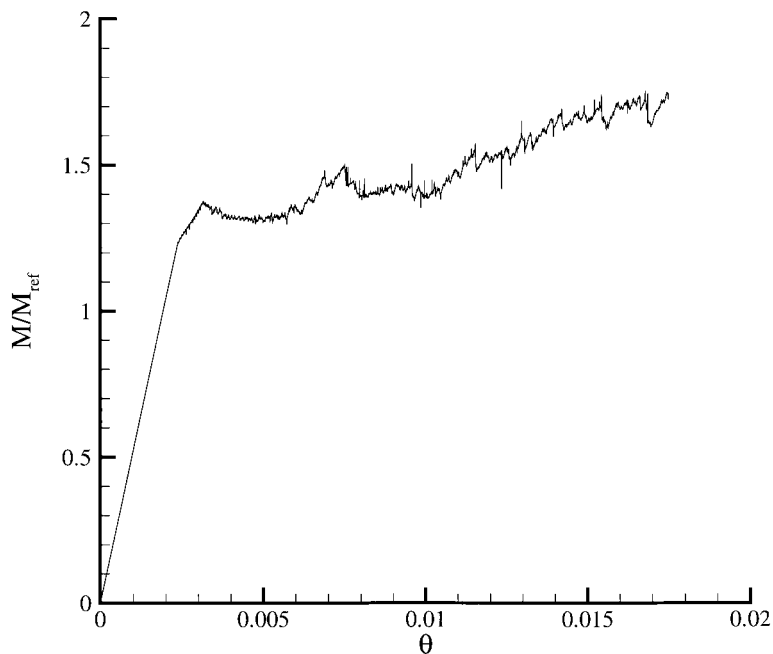


Fig. 4. Moment versus rotation angle for the reference case.

The first dislocation activity occurs when M/M_{ref} is ≈ 1.24 and the deviation from the elastic slope is evident in Fig. 4 $M/M_{\text{ref}} = 1.26$. Assuming that the moment at initial yield is related to the yield strength σ_y by $M_y = 2\sigma_y(h/2)^2/3$, this corresponds to $\sigma_y \approx 62$ MPa. After initial yielding, the moment increases until a local maximum is reached ($M/M_{\text{ref}} = 1.37$), decreases to a local minimum ($M/M_{\text{ref}} = 1.31$) and subsequently tends to increase, with fluctuations that arise from discrete dislocation events.

The evolution of the dislocation distribution is shown in Fig. 5. The distribution of sources shows that the slip planes are chosen so that none intersect the ends, $x_1 = \pm L/2$, where displacement boundary conditions are prescribed. The dislocations are arranged in arrays of positive dislocations on slip systems that are at $+30^\circ$ from the x_1 -axis and arrays of negative dislocations on slip systems that are at -30° from the x_1 -

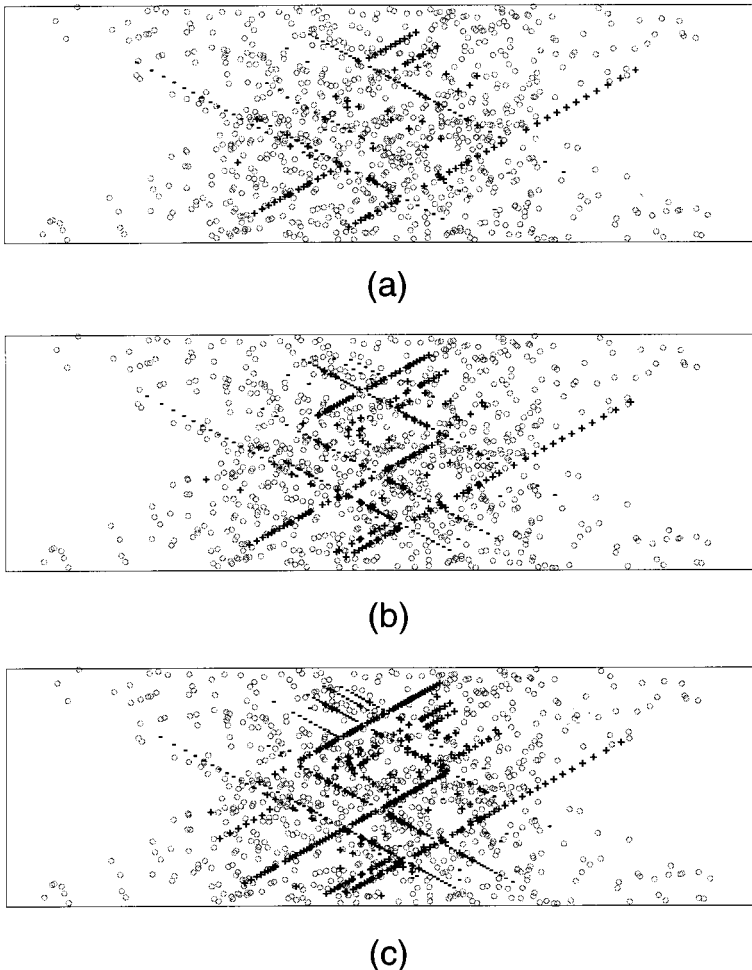


Fig. 5. Dislocation distribution for the reference case. (a) $\theta = 0.01$; (b) $\theta = 0.0125$; (c) $\theta = 0.0175$. Sources are denoted by a gray o, while the + and – symbols denote signed dislocations using the sign convention of Fig. 2.

axis (see Fig. 2 for the sign convention used here). Since dislocations are generated as dipoles, this implies that opposite signed dislocations on each of these slip systems have exited the specimen through one of the free surfaces. The rotation that arises from each set of dislocation arrays has the sense that is “geometrically necessary” for the imposed θ . However, not all the dislocations on these slip systems are geometrically necessary. Due to the internal stress built up in the crystal a few dislocations have even nucleated on the third slip system that has $\varphi = +90^\circ$. At the stage shown in Fig. 5(a) $\theta = 0.01$ which is while the moment versus curvature relation in Fig. 4 is still rather flat. Between Figs. 5(b) and (c), there is a significant increase in the moment. The development of high dislocation densities on intersecting slip systems creates barriers to dislocation motion, which gives rise to this hardening.

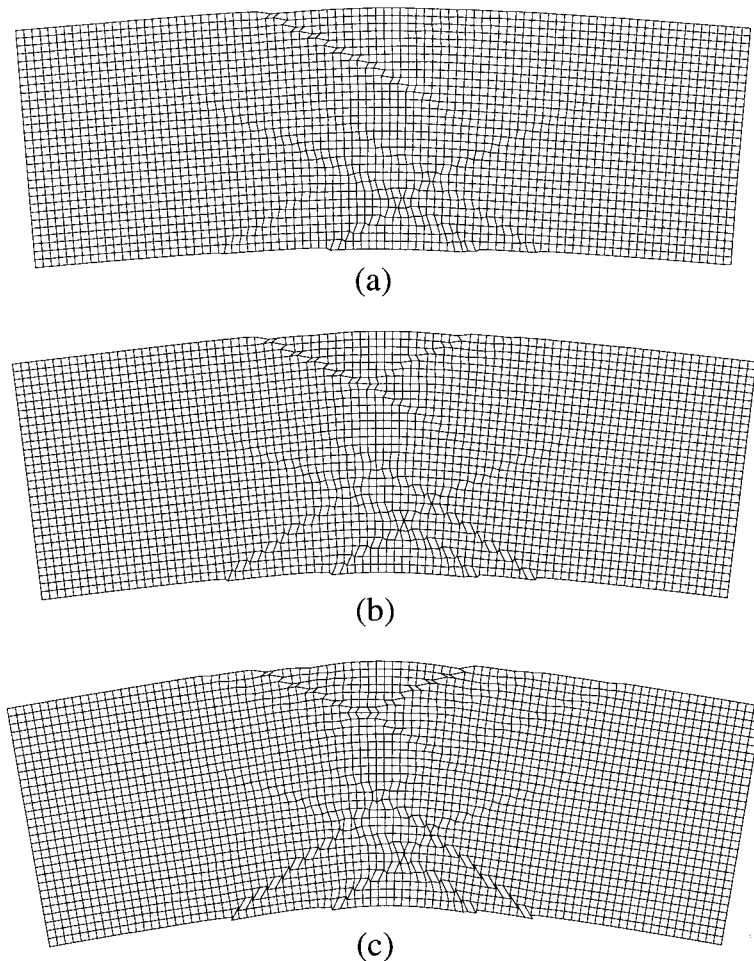


Fig. 6. Deformed finite element meshes for the reference case. Displacements are multiplied by 10: (a) $\theta = 0.00863$. (b) $\theta = 0.0122$. (c) $\theta = 0.0175$.

The deformations that result are shown in Fig. 6. The slip steps that develop on the free surfaces can be seen. The highly localized deformations are a consequence of the discrete dislocation distribution. Since the highly localized deformations are associated with the discrete dislocations, which are represented analytically, the fact that these deformation fields are concentrated in a row of elements does not indicate a mesh dependence of the results (such a mesh dependence would be the case for localization of deformation in a rate independent continuum); it is simply an indication of how highly localized the displacement fields are for an array of discrete dislocations. Indeed, the wavelengths associated with gradients in the ($\hat{\cdot}$) fields that are solved for by the finite element method are long with respect to the mesh length.

This can be clearly seen in Fig. 7(a) which shows contours of $\hat{\sigma}_{11}$ at $\theta = 0.0175$. The “image” stress is tensile at the top of the specimen and compressive at the bottom. This field is very smoothly varying and is readily resolved by the finite element mesh.

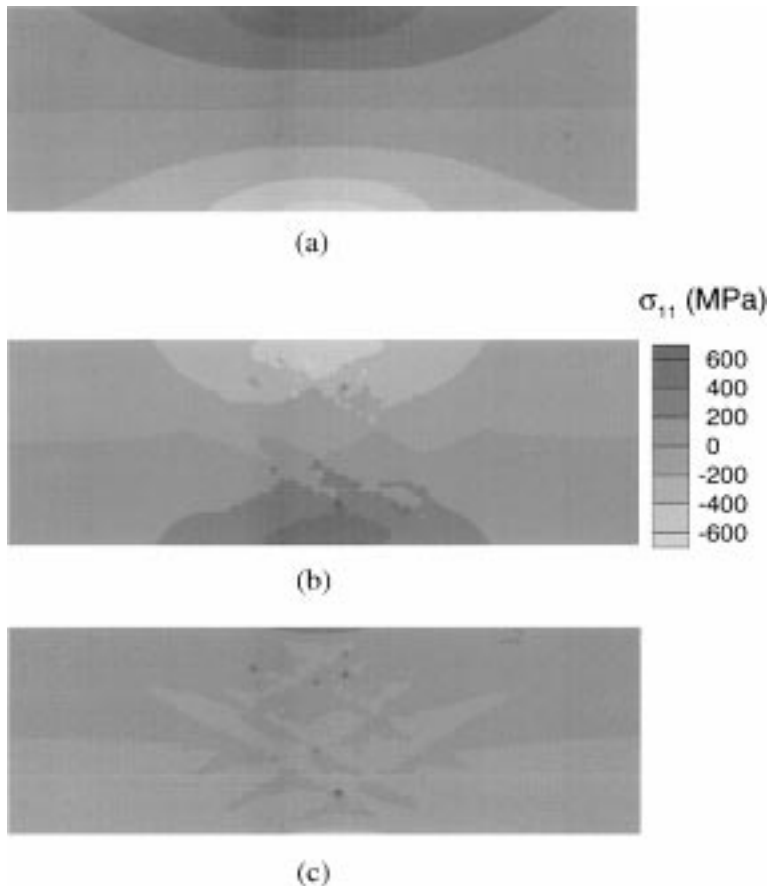


Fig. 7. Stress contours for the reference case at $\theta = 0.0175$: (a) the image stress $\hat{\sigma}_{11}$; (b) the dislocation stress $\tilde{\sigma}_{11}$. (c) the total stress $\sigma_{11} = \hat{\sigma}_{11} + \tilde{\sigma}_{11}$.

Also, note the resemblance of the image distribution of $\hat{\sigma}_{11}$ to the elastic distribution in Fig. 3(b). Contours of the discrete dislocation stress $\tilde{\sigma}_{11}$ at the same instant are shown in Fig. 3(b). Of course, each dislocation generates a singular stress field that decays inversely proportional with the distance, but since the stresses are extrapolated to the nodes of the finite element mesh, this is not visible in this plot. The collective dislocation structure gives rise to a high tensile stress at the bottom of the specimen and to a high compressive stress at the top. Contours of the total $\sigma_{11} = \hat{\sigma}_{11} + \tilde{\sigma}_{11}$ are shown in Fig. 7(c). Since the discrete dislocation $\tilde{\sigma}_{11}$ and image $\hat{\sigma}_{11}$ fields are of opposite sign over much of the specimen, the total stress is reduced.

The mesh dependence of the moment–rotation curve is shown in Fig. 8 where results using the reference 90×30 mesh and a coarser 46×16 mesh are presented. Initially, the two curves coincide, but after a rotation of about 0.006, the coarser mesh gives a somewhat higher moment. This is the result of several factors. One, of course, is the resolution of the $(\hat{\cdot})$ fields themselves. Another is that with the coarser mesh, the nodal values of $\tilde{\sigma}_{ij}$, which provide the loading term for the $(\hat{\cdot})$ fields, provide a less accurate discretization. Finally, there is the reduced accuracy associated with having fewer integration points in Eq. (12) to integrate the stress field along $x_1 = \pm L/2$.

In classical plasticity, the moment versus rotation relation in bending is a direct outcome of the tensile stress versus strain relation. Within the discrete dislocation context, the relation between the tensile stress–strain response and the bending moment–rotation relation is not so straightforward, because of the different dislocation structures that develop. To illustrate this, Figs. 9 and 10 and show the result of

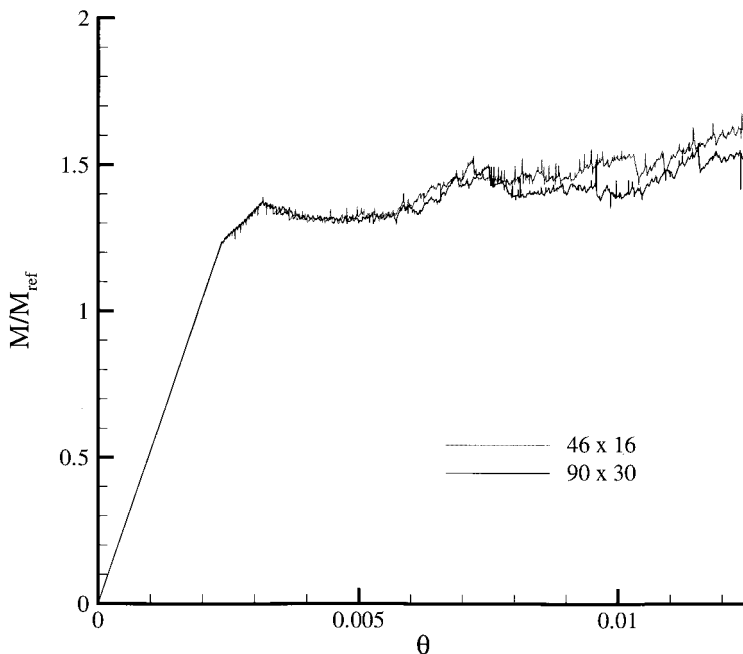


Fig. 8. Moment versus rotation angle for the reference case using two finite element discretizations.

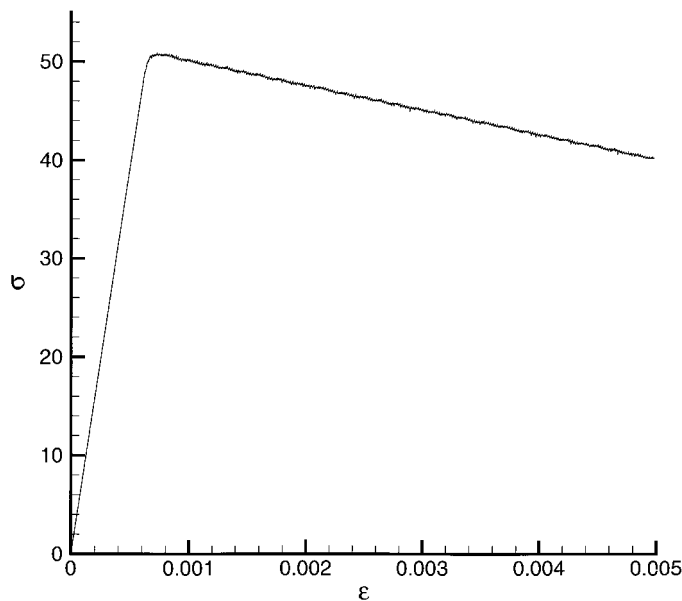


Fig. 9. Stress versus strain in plane strain tension for the reference specimen.

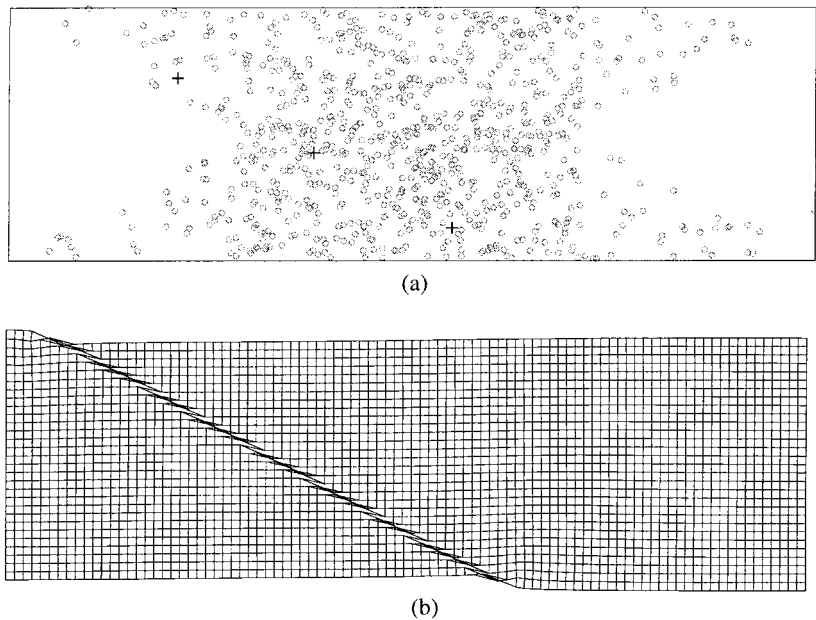


Fig. 10. (a) Dislocation distribution for the reference specimen in plane strain tension at $\epsilon=0.0104$. Sources are denoted by a gray o, while the + and – symbols denote signed dislocations using the sign convention of Fig. 2; (b) deformed mesh for the reference specimen in plane strain tension at $\epsilon=0.0104$. Displacements are multiplied by 10.

subjecting the reference specimen to plane strain tension, with the loading axis corresponding to the x_1 -axis. The boundary conditions that are used are stress free surfaces at $x_2 = \pm h/2$ and a prescribed uniform tensile u_1 displacement and vanishing shear stress at $x_1 = \pm L/2$. In Fig. 9 $\sigma = \sigma_{11}$ and $\varepsilon = \varepsilon_{11}$. The first dislocation activity in Fig. 9 occurs at $\sigma = 49$ MPa, which is a smaller value of stress than the one deduced from the value of M at the initiation of dislocation activity in Fig. 4. This is a consequence of the different stress distributions in tension and bending in conjunction with the statistical distribution of dislocation source strengths. In tension, a peak stress is reached at ≈ 51 MPa and the stress subsequently decreases monotonically. The deformed mesh in Fig. 10(b) shows that plastic flow has localized on one slip plane. The very low dislocation density seen in Fig. 10(a) arises because the dislocations that are nucleated exit the specimen at the free surfaces $x_2 = \pm h/2$. The strong localization and associated softening in plane strain tension is due to the lack of dislocation obstacles in the reference specimen.

3.2. Effect of slip geometry

The effect of variations in the number of sources and the number of slip systems is seen in Fig. 11. The first case is the one shown previously in Fig. 4 with a slip plane spacing of $100 b$, while cases 2 and 3 correspond to a spacing of $50 b$. Case 2 has the

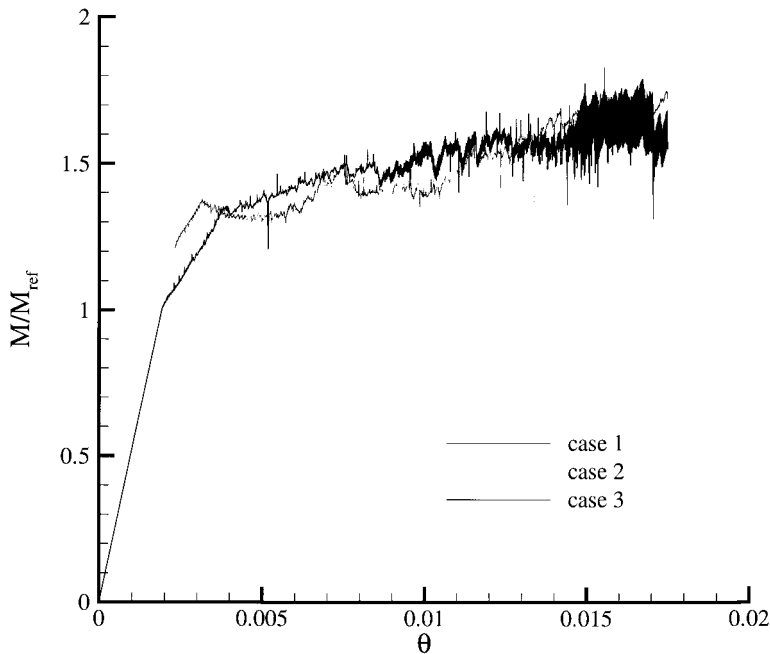


Fig. 11. The effect of slip plane spacing and source density on the moment versus rotation angle. Cases 2 and 3 use a two times finer slip plane spacing than case 1, the reference case. Case 2 has a two times higher source density than case 1. Case 3 has the same source density as case 1.

same number of sources per slip plane, leading to a total of 1618 sources, while case 3 has only half the number of sources per plane, totalling 809 sources just as in case 1. The responses for case 2 and especially case 3 exhibit rather wild oscillations from around $\theta = 0.01$. This is caused by high-frequency dislocation nucleation–annihilation cycles: a number of sources are generating new dipoles which annihilate shortly afterwards because they cannot survive inside the existing complex stress field due to all dislocations. This process repeats itself almost every t_{nuc} s during the latter stages for case 3. Similar processes have also occurred in some of the other cases to be discussed, and in these cases we have often stopped the calculation.

It is seen from Fig. 11 that, apart from the initiation of plasticity, the global response is not very sensitive to the slip plane spacing. In fact, as can be appreciated from Fig. 5, the spacing between active slip planes is significantly larger than that between potential slip planes. The initiation of plasticity caused by the motion of the first generated dislocations obviously depends quite strongly on the density of dislocation sources and the position of the low-strength sources relative to the outer fibers of the specimen. These results suggest that the initial yield point is a stochastic quantity to a certain extent, whereas the ultimate bending moment is determined largely by the average source strength.

A case where the only slip system is the one at $\varphi = +30^\circ$ is shown in Fig. 12. The slip plane and source distribution is identical to that for the $\varphi = +30^\circ$ slip system in Fig. 4, and the reference case curve from this figure is included for comparison

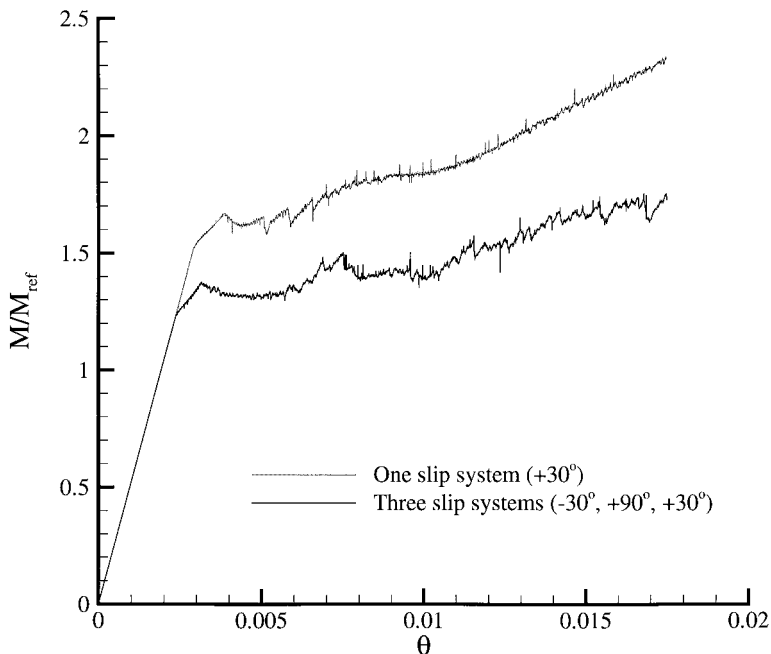


Fig. 12. The effect of the number of slip systems on the moment versus rotation angle curve. The case with three slip systems is the reference case.

purposes. With one slip system, the first dislocation activity is at $M/M_{\text{ref}} = 1.52$, which using $M_y = 2\sigma_y(h/2)^2/3$, corresponds to a yield strength of about 76 MPa. A local maximum is reached which is then followed by a local minimum as for the three slip system case. However, subsequently, the one slip system bending moment versus rotation curve has a distinctly higher slope than does the reference case.

The dislocation distributions and the deformed meshes for both cases at $\theta = 0.0175$ are compared in Figs. 13 and 14, respectively. When there is only one slip system at 30° , only dislocations of the same sign are seen in the specimen, Fig. 13(b). As a consequence, the deformed mesh in Fig. 14(b) only shows bands of localized deformation in one direction.

Fig. 15 shows the evolution of the dislocation density for these two cases. The density of geometrically necessary dislocations is given by Nye (1953) and Ashby (1970) as

$$\rho_G = \frac{k^p}{b_1} = \frac{2\theta^p}{Lb_1} \quad (22)$$

where k^p is the plastic curvature, θ^p is the plastic rotation and b_1 is the component of the Burgers vector parallel to the x_1 – axis, $b_1 = b \cos \varphi$, where φ is defined in Fig. 2. In Eq. (22) θ^p is the average of the angle change over the height of the strip which is induced by edge dislocations situated at a distance x_2 from the middle surface (see Eshelby, 1962; Siems et al., 1962). The relation Eq. (22) implies that the density of

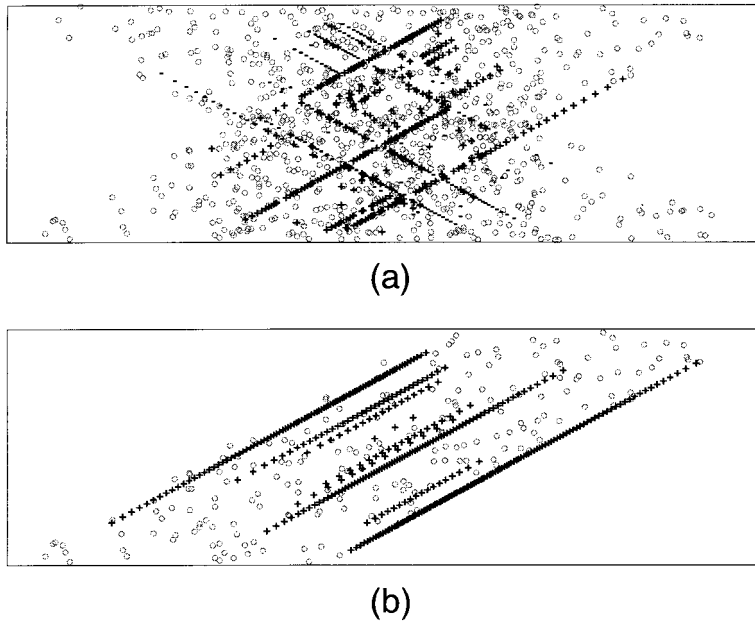


Fig. 13. Dislocation distribution for: (a) the reference case at $\theta = 0.0175$; (b) the case with one slip system at 30° at $\theta = 0.0175$. Sources are denoted by a gray o, while the + and – symbols denote signed dislocations using the sign convention of Fig. 2.

geometrically necessary dislocations increases linearly with the rotation θ^p . The plastic rotation is given by $\theta^p = \theta - \theta^e$, where the elastic rotation for plane strain bending is related to the moment through

$$M = \frac{Eh^3}{12(1-\nu^2)} \left(\frac{2\theta^e}{L} \right) = \frac{Eh^3}{12(1-\nu^2)} k^e = Dk^e \quad (23)$$

with k^e being the elastic curvature and D the bending stiffness.

From Eq. (23), for the case with one slip system in Fig. 15, $\theta^e = 0.29 \times 10^{-2}$ at initial yield, while $\theta^e = 0.45 \times 10^{-2}$ at the last stage of deformation, $\theta = 1.75 \times 10^{-2}$. Thus, the change in θ for $\theta \gg 0.004$ is nearly entirely a change in θ^p so that the linearity seen in Fig. 15 for the calculation with one slip system also reflects a linear dependence of the dislocation density on θ^p . To make a more quantitative comparison, at $\theta = 1.75 \times 10^{-2}$ we obtain the density of dislocations from Fig. 15 as $8.4 \times 10^{12} \text{ m}^{-2}$. Using $\theta^p = \theta - \theta^e = 1.30 \times 10^{-2}$, the density of geometrically necessary dislocations is $10 \times 10^{12} \text{ m}^{-2}$. To understand how Eq. (22) can give a dislocation density greater than the one in the specimen, we note that the density of geometrically necessary dislocations can be written as $\rho_G = n_G/(Lh)$ so that Eq. (22) implies

$$n_G = \frac{2\theta^p h}{b_1} \quad (24)$$

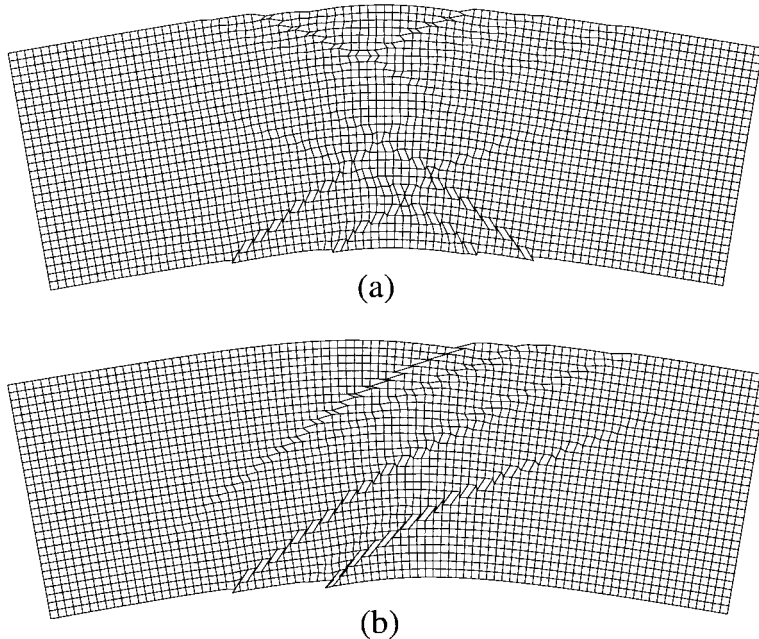


Fig. 14. Deformed finite element meshes for: (a) the reference case at $\theta = 0.0175$; (b) the case with one slip system at 30° at $\theta = 0.0175$. Displacements are multiplied by 10.

which, however, presumes that the dislocations extend over the full height h of the strip. As can be seen in Fig. 13(b), there is a dislocation-free layer at the top and bottom of the strip. The dislocations extend only over a height of $3.36 \mu\text{m}$ (or $0.84h$) and substituting this effective height for h in calculating the number of geometrically necessary dislocations accounts for the discrepancy.

For the reference case, with three slip systems, $\theta^e = 0.33 \times 10^{-2}$ at $\theta = 1.75 \times 10^{-2}$ so that $\theta^p = 1.42 \times 10^{-2}$. This corresponds to $\rho_G = 10.9 \times 10^{12} \text{ m}^{-2}$. Accounting for the dislocation free layers at the top and bottom of the specimen, as was done for the single slip system case, gives an effective height of $3.57 \mu\text{m}$ and a corrected ρ_G value of $9.7 \times 10^{12} \text{ m}^{-2}$. The actual value of the dislocation density is $15.6 \times 10^{12} \text{ m}^{-2}$ which is significantly larger than ρ_G . Hence, about one third of the dislocations in Fig. 5(c) are “statistical” rather than geometrically necessary. The local stress fields from dislocations on one slip system activate sources on other slip systems to generate dislocations that are not geometrically necessary.

The effect of changing the angle of the slip systems with respect to the x_1 -axis is shown in Figs. 16 and 17. With $\phi = \pm 60^\circ$ only two slip systems are present. The same number of sources per slip plane is specified as in the reference case. Because with $\phi = 60^\circ$, the slip plane length is shorter than in the reference case, the source spacing is smaller. A symmetrically located third system would be parallel to the x_1 -axis, which would lead to possible computational complications arising from dislocations exiting

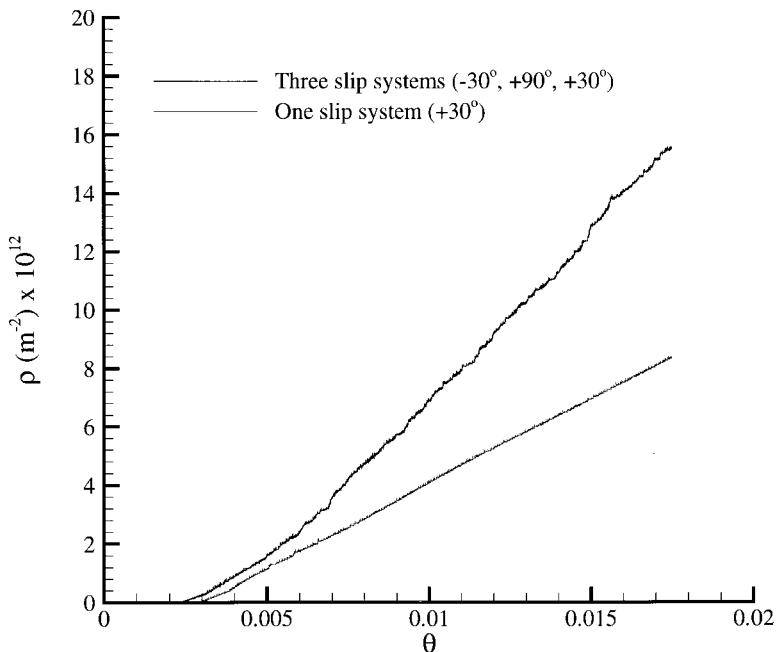


Fig. 15. The effect of the number of slip systems on the evolution of the dislocation density ρ . The case with three slip systems is the reference case.

the specimen along the edges where bending is prescribed. The first dislocation activity occurs at $M/M_{\text{ref}} = 0.70$. Subsequently, there is an initial interval of rather high hardening until $M/M_{\text{ref}} \approx 0.9$. Then, the trend of the moment versus rotation relation is similar to that for the reference case except that the hardening is somewhat less.

The dislocation distribution in Fig. 17 mainly consists of arrays of positive dislocations on the slip systems at $+60^\circ$ and arrays of negative dislocations on the slip systems at -60° although some dislocations that do not follow this trend are also found. The deformed finite element mesh in Fig. 17(b) shows the highly localized deformations that are a consequence of the dislocation arrays.

3.3. Effect of obstacles

The effect of obstacles on the moment versus rotation relation is shown in Fig. 18. For the three slip system case in Fig. 18(a), dislocation activity begins at $M/M_{\text{ref}} = 1.23$ both with and without obstacles (cf. Figs. 4–7) present. When obstacles are present, the initial hardening rate is higher but at larger rotations there is no systematic difference in hardening rate between the calculations with and without obstacles. For $\theta > 0.01$, the value of the moment with obstacles is 10–20% higher than without obstacles. With slip systems at $\varphi = \pm 60^\circ$, [Fig. 18(b)], the first dislocation activity begins at $M/M_{\text{ref}} = 0.69$ both with and without obstacles (cf. Figs. 16

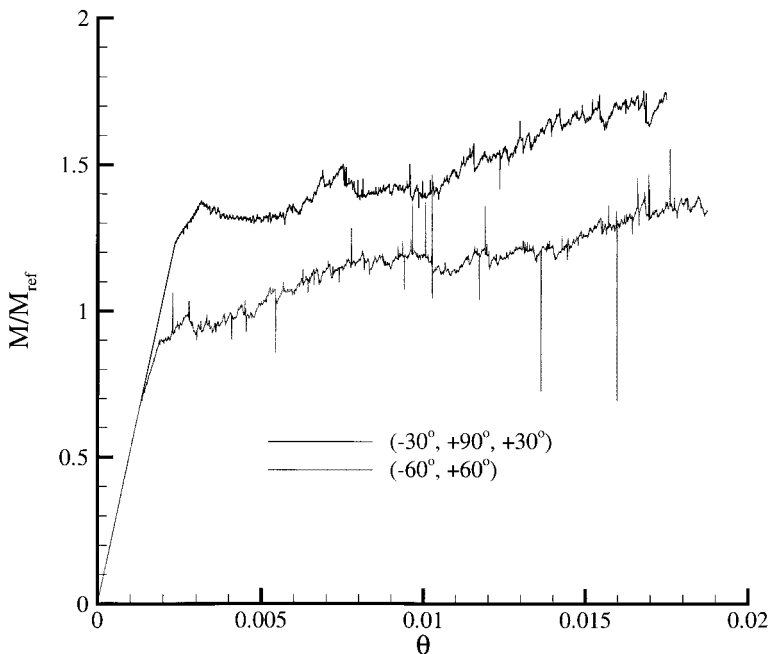


Fig. 16. The effect of slip plane orientation φ on the moment versus rotation angle. The case labeled $(+30^\circ, 90^\circ, -30^\circ)$ is the reference case.

and 17) present. However, here the obstacles succeed in blocking the initial dislocations that are generated until they are annihilated by opposite signed dislocations from another nucleation event. As a consequence, the slope of the moment versus rotation curve is not noticeably altered. Subsequent nucleation–annihilation events give rise to the small dips in the moment versus rotation curve that can be seen in Fig. 18(b). The moment attains a much higher value with obstacles present, about 70% greater than the corresponding case without obstacles, but softening then ensues and for the larger values of θ , the moment for the calculation with obstacles present is about 25% above the value for the calculation with no obstacles. Oscillations in the moment associated with nucleation–annihilation events are evident for the calculation with obstacles.

Fig. 19 shows the evolution in the dislocation density for the cases with slip systems at $\varphi \pm 60^\circ$ in Fig. 18(b). The evolution of the total dislocation density in Fig. 19(a) shows that, with obstacles present the total dislocation density is initially smaller than without obstacles present, because of the dislocation pinning and annihilation activity mentioned above. The total dislocation density with obstacles present overtakes that for the calculation without obstacles at $\theta \approx 0.004$ which coincides with the moment decreasing from its peak value in Fig. 18(b). Fig. 19(b) shows the evolution of the mobile dislocations, i.e. the ones not pinned at an obstacle. The much greater initial density of mobile dislocations in the absence of obstacles is even more clearly seen in this plot. At larger values of θ , the mobile dislocation density is essentially the same whether or not obstacles are present.

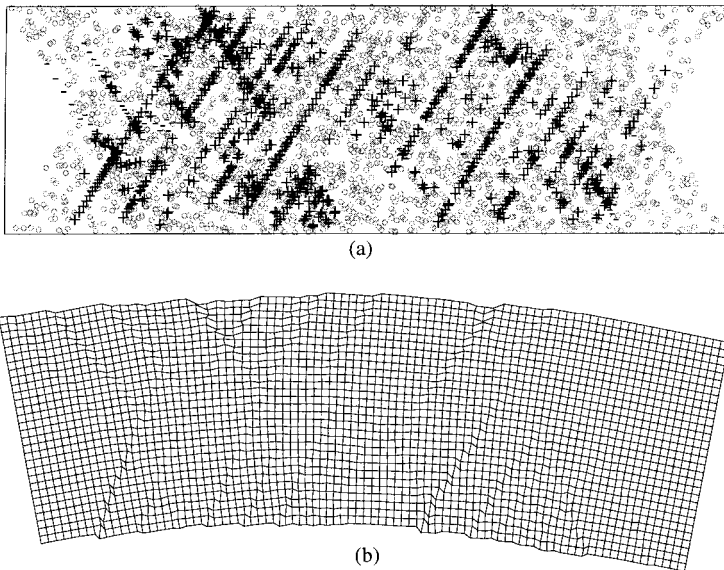


Fig. 17. (a) Dislocation distribution for the case with slip systems at $\varphi = \pm 60^\circ$ to the x_1 -axis at $\theta = 0.0188$. Sources are denoted by a gray o, while the + and - symbols denote signed dislocations using the sign convention of Fig. 2; (b) deformed finite element mesh for the case with slip systems at $\varphi = \pm 60^\circ$ to the x_1 -axis at $\theta = 0.0188$. Displacements are multiplied by 10.

Similar curves (not shown here) of total and mobile dislocation density versus rotation for the calculations with three slip systems in Fig. 18(a) show a slightly different trend. In the initial stages of bending, the total dislocation densities are very similar for these two cases, consistent with the lack of nucleation-pinning-annihilation events for the $(+30^\circ, +90^\circ, -30^\circ)$ slip system calculation with obstacles present. With increasing θ , the total dislocation density with obstacles gradually becomes greater than for the calculation with no obstacles (the reference case). The mobile dislocation densities are essentially equal up to $\theta \approx 0.007$ after which the mobile

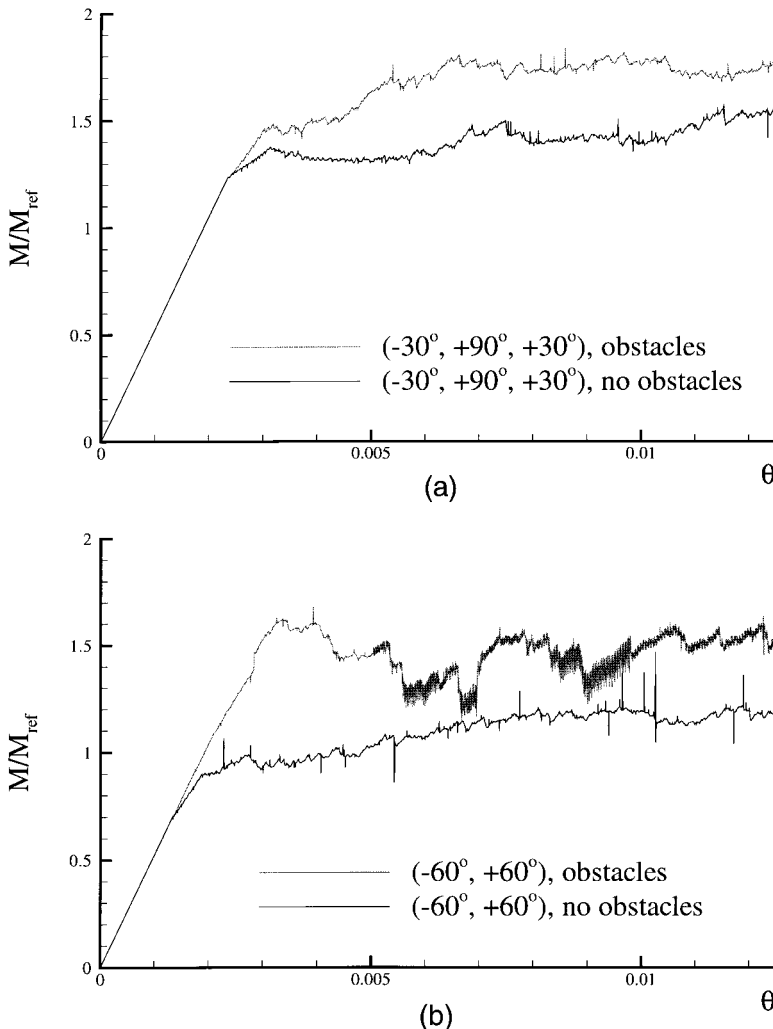


Fig. 18. The effect of obstacles on the moment versus rotation angle: (a) for three slip systems at $(-30^\circ, +90^\circ, +30^\circ)$. The case with no obstacles is the reference case; (b) for two slip systems at $(-60^\circ, +60^\circ)$.

dislocation density for the calculation with obstacles is slightly greater than when no obstacles are present.

3.4. Size effects

We now consider the effect of specimen size on the bending response of the strip. Fig. 20 shows the response of specimens that are $12 \times 4 \mu\text{m}$ (the reference case), $24 \times 8 \mu\text{m}$ and $48 \times 16 \mu\text{m}$. There are three slip systems at $(-30^\circ, +90^\circ, +30^\circ)$ with the

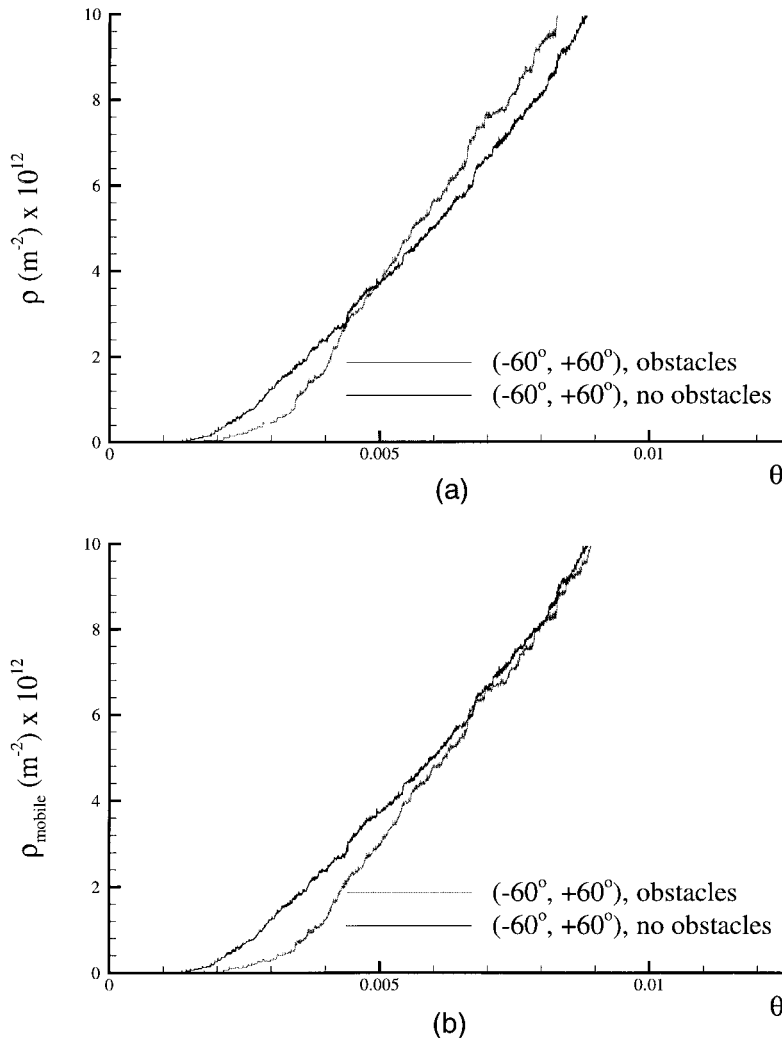


Fig. 19. The effect of obstacles on the evolution of the dislocation density for two slip systems at $(-60^\circ, +60^\circ)$: (a) total dislocation density; (b) mobile dislocation density.

same spacing of $100b$ and no obstacles. All specimens have the same source density with random source distributions generated for all cases independently, so that there will be some statistical differences in addition to differences due to size. The same rotation rate $\dot{\theta}$ is prescribed in all three calculations. The meshes for the two larger specimens have 180×60 quadrilateral elements. The moment versus rotation response is shown in Fig. 20(a) and the dislocation density, ρ , versus plastic curvature, κ^p , is shown in Fig. 20(b). Since the specimens are geometrically similar, i.e. have the same h/L ratio, the normalization of the moment is such that the normalized moment versus rotation curves for the three specimens would coincide if a conventional size-independent continuum theory were used. The plastic curvature is computed at each stage of the deformation from $\kappa^p = \kappa - \kappa^e$ or, using Eq. (23),

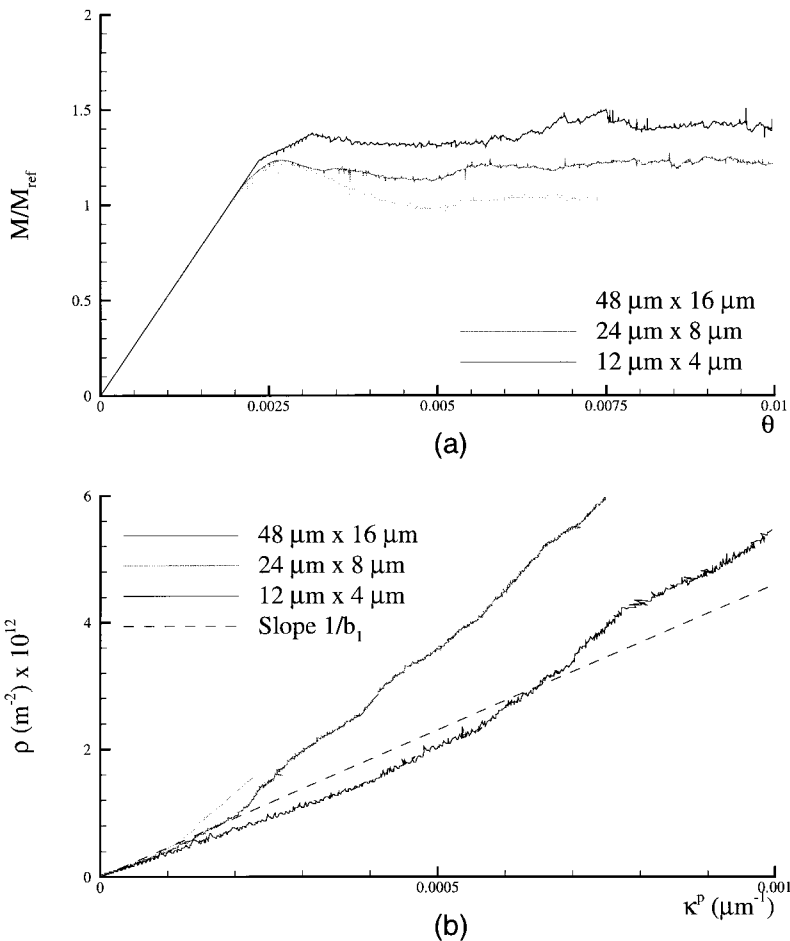


Fig. 20. The effect of size with three slip systems at $(-30^\circ, +90^\circ, +30^\circ)$. (a) moment versus rotation angle; (b) dislocation density versus plastic curvature. The case labeled “ $12 \mu\text{m} \times 4 \mu\text{m}$ ” is the reference case.

$$\kappa^p = \frac{2\theta}{L} - \frac{M}{D} \quad (25)$$

From Eq. (22), the relation between ρ and κ^p would be a straight line with slope $1/b_1$ if all the dislocations were geometrically necessary. For comparison purposes, a line with this slope is plotted in Fig. 20(b).

The initial deviation from the linear elastic slope in Fig. 20(a) occurs at about the same point for the two larger specimens and somewhat later for the smallest specimen (the reference case). However, for $\theta > 0.003$, the values of the moment become ordered monotonically according to size with the smallest specimen having the highest value of the moment at a given rotation. In Fig. 20(b), the dislocation density versus plastic curvature response is linear with a slope that is 10–15% smaller than $1/b_1$. Although not evident on the scale of Fig. 20(b), at a given value of the plastic curvature κ^p , the dislocation density generally increases monotonically with specimen size. This is consistent with the existence of a dislocation-free layer near the free surfaces as discussed in reference to Fig. 15, the relative effect of which decreases with increasing specimen height. The larger the specimen, the smaller the value of κ^p at which deviation from the linear slope occurs. Since the dislocation density is greater than geometrically necessary, by definition, the increase in dislocation density is

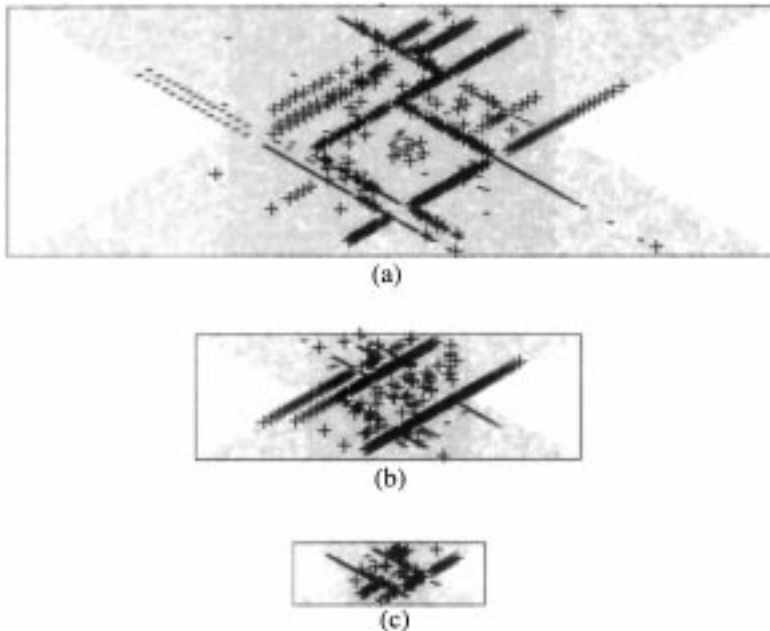


Fig. 21. Dislocation distributions for the three sizes in Fig. 20 at a rotation of $\theta = 0.0075$: (a) $48 \times 16 \mu\text{m}$; (b) $24 \times 8 \mu\text{m}$; (c) $12 \times 4 \mu\text{m}$ (the reference case). Sources are denoted by a gray o, while the + and – symbols denote signed dislocations using the sign convention of Fig. 2.

associated with statistical dislocations. In tension, there are no geometrically necessary dislocations and a plane strain tension calculation carried out for the $24 \times 8 \mu\text{m}$ specimen, as shown in Figs. 9 and 10 for the reference specimen, indeed showed no size effect.

Fig. 21 compares the dislocation distributions in the three differently sized specimens at the same rotation. One notices that the spacing between the active slip planes that are heavily populated with dislocations, which we will here call slip bands, decreases with decreasing size. Although the identification of slip bands is somewhat arbitrary, we have estimated the average spacing between slip bands to be $0.8 \mu\text{m}$ for the $12 \times 4 \mu\text{m}$ reference case, $1.6 \mu\text{m}$ for the case of $24 \times 8 \mu\text{m}$ and $2.6 \mu\text{m}$ for a size of $48 \times 16 \mu\text{m}$. For the smallest two specimens, these values scale with the specimen size, while for the largest one it is slightly smaller than scaling would imply. These scaling properties can be understood in terms of geometrically necessary dislocations as follows. According to Eq. (24), the number of geometrically necessary dislocations at the same plastic rotation θ^p scales directly with the height h of the specimen. However, the maximum number of dislocations on any one slip plane is limited by the spacing of dislocations in the pile up. If one assumes that this dislocation spacing is constant, the maximum number of dislocations per slip plane increases linearly with specimen size too. As a consequence, the number of slip bands is independent of specimen size, so that the mean slip band spacing is proportional to

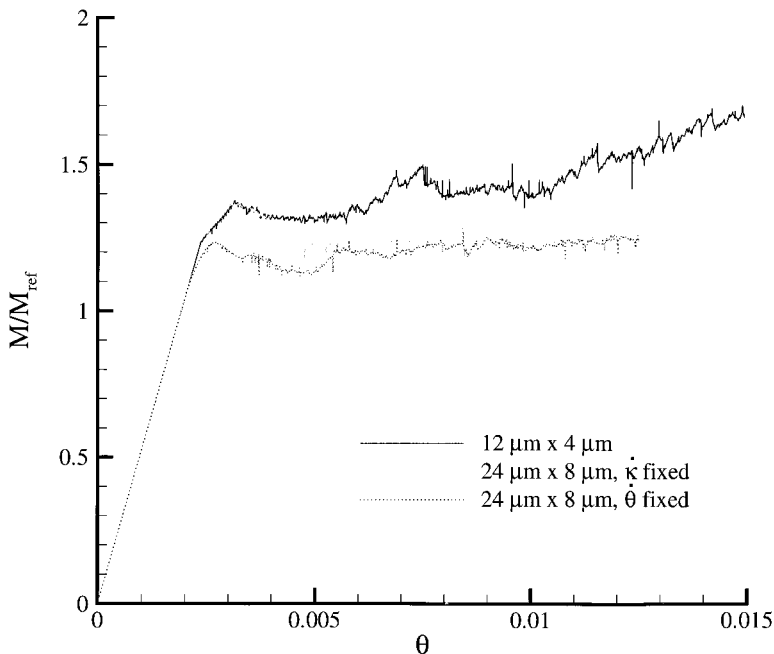


Fig. 22. The effect of size and loading rate on the moment versus rotation angle. The case labeled “ $12 \mu\text{m} \times 4 \mu\text{m}$ ” is the reference case.

size. The fact that the larger specimen has a smaller spacing can be attributed to the substantial number of statistical dislocations.

As an alternative to applying the same rotation rate $\dot{\theta}$, the same curvature rate, $\dot{\kappa} = 2\dot{\theta}/L$, could be prescribed for the different sized specimens. The responses are expected to be somewhat different since the discrete dislocation model is inherently rate dependent, which results from the drag force on dislocation motion in Eq. (8) and from the time scale for dislocation nucleation. Fig. 22 compares the moment versus rotation response of the $24 \times 8 \mu\text{m}$ specimen loaded with the same $\dot{\theta}$ and with the same $\dot{\kappa}$ as the reference specimen. The initial plastic response is highly rate dependent. However, after the initial yield phenomena, the values of the moment for the two $24 \times 8 \mu\text{m}$ calculations are within 5–7%. Initially, at low dislocation densities

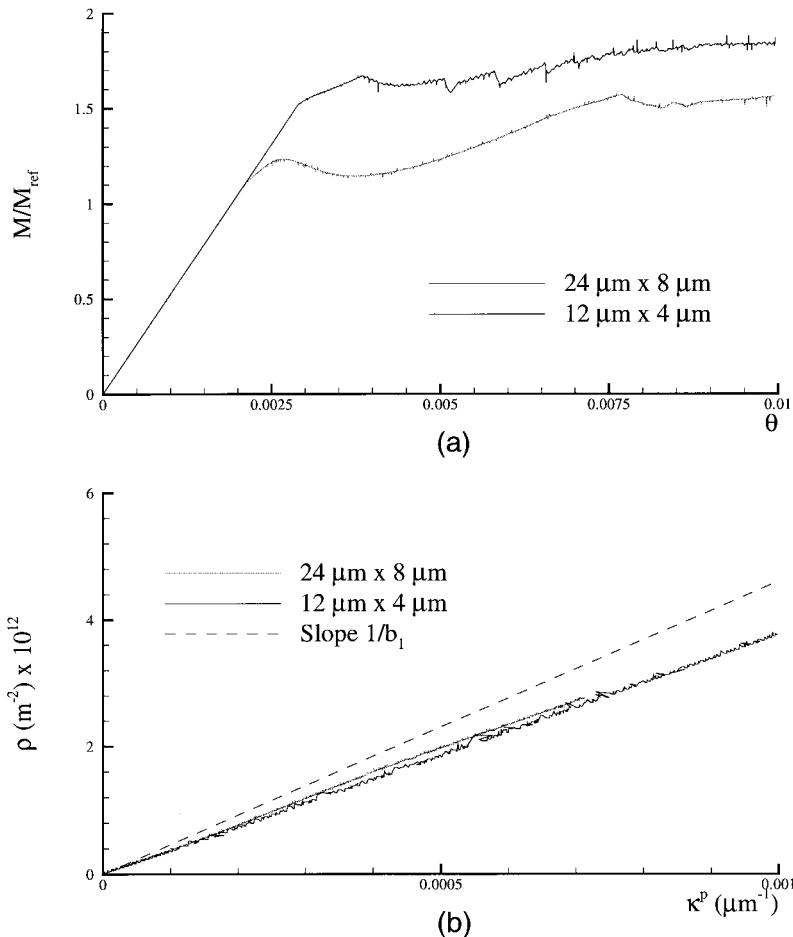


Fig. 23. The effect of size with one slip systems at $(+30^\circ)$: (a) moment versus rotation angle; (b) dislocation density versus plastic curvature. The case labeled “ $12 \mu\text{m} \times 4 \mu\text{m}$ ” is the reference case.

the rate dependence associated with dislocation drag dominates, while at higher densities the rate dependence is mainly that associated with dislocation nucleation.

Fig. 23 shows the effect of specimen size on the bending response when there is one slip system at $\varphi + 30^\circ$. In this case, the slope of the dislocation density versus plastic curvature is linear for both specimens over the range calculated. The dislocation density is slightly larger for the larger specimen. As already noted, the deviation from a slope of $1/b_1$ arises from dislocation-free layers near the free surface. As expected, this effect reduces somewhat with increasing specimen size. In Fig. 23(a), the moment for the smaller specimen in the initial stages of plastic flow, $\theta < 0.005$, is up to 45% higher than that for the smaller specimen. For $\theta > 0.005$, the difference in moment, at a given value of θ , between the two specimens is 15–20%.

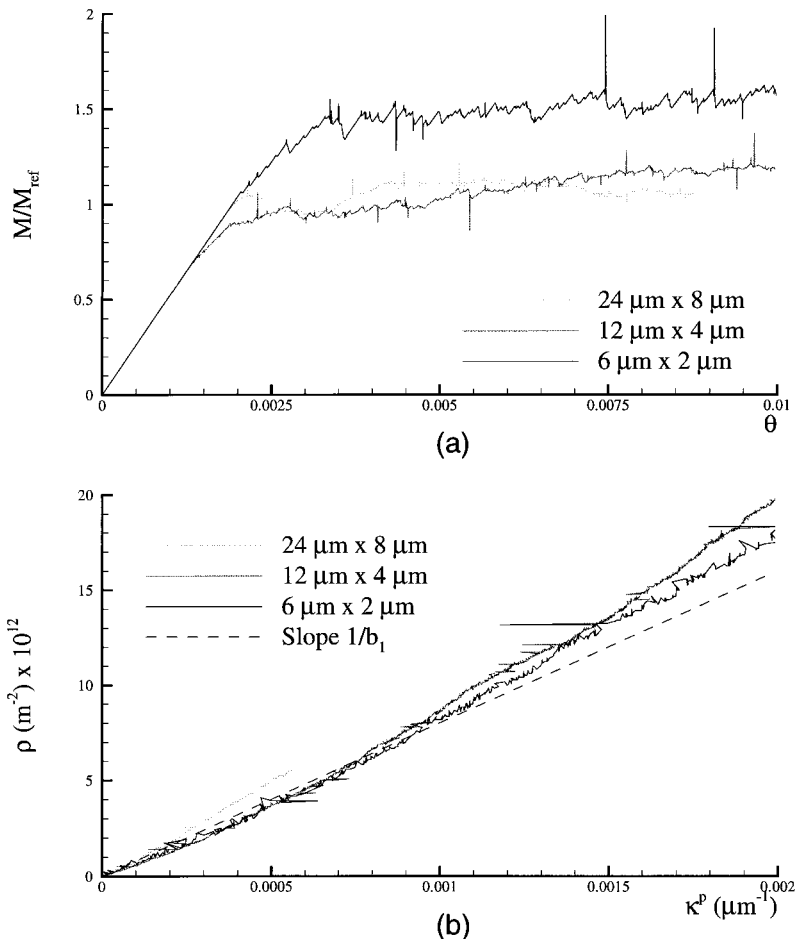


Fig. 24. The effect of size with two slip systems at $(-60^\circ, +60^\circ)$: (a) moment versus rotation angle; (b) dislocation density versus plastic curvature. The case labeled “12 $\mu\text{m} \times 4 \mu\text{m}$ ” is the reference case.

In this range, the size effect on the moment versus rotation curves in Fig. 23(a) is similar to that in Fig. 20(a). The dislocation density for the larger specimen in Fig. 20(b) is much larger than for the smaller specimen, whereas in Fig. 23(b) the dislocation densities for the $24 \times 8 \mu\text{m}$ and $12 \times 4 \mu\text{m}$ specimens are nearly the same. This indicates that the size effect is dominated by the geometrically necessary dislocations. The dislocation distributions (not shown) again show that the mean slip band spacing scales rather well with the specimen size, in agreement with the argument put forward in relation to Fig. 21.

In Fig. 24 the size effect on the bending response of a specimen with two slip systems at $\varphi = 60^\circ$ is shown, again with the same prescribed rotation rate $\dot{\theta}$. Instead of a large specimen of $48 \times 16 \mu\text{m}$, the third size considered here is a small $6 \times 2 \mu\text{m}$ specimen. The initial yielding is again dominated by statistical effects but well into the plastic regime, for $\theta > 0.0065$, the bending moment tends to be smaller for the larger specimens. The increase in dislocation density with specimen size in Fig. 24(b) is consistent with what occurred for the specimens with three slip systems at $(-30^\circ, +90^\circ, +30^\circ)$. The dislocation structures that result for the different specimens at the same rotation are shown in Fig. 25. The slip band spacings estimated from this figure are 1, 0.7 and $0.3 \mu\text{m}$, ordered from the large to the small specimen, and obey roughly the same scaling with h as in the previous cases with one or three slip systems.

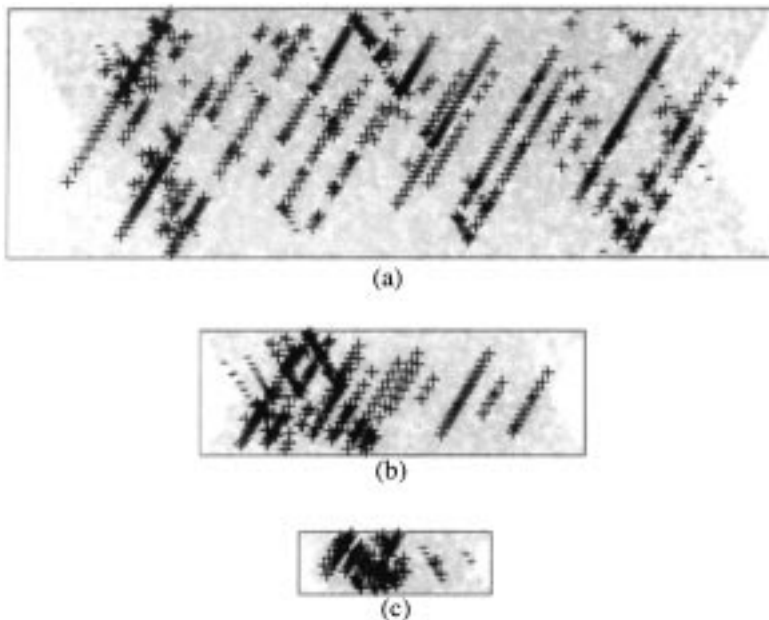


Fig. 25. Dislocation distributions for the cases in Fig. 24 at $\theta = 0.01$: (a) $24 \mu\text{m} \times 8 \mu\text{m}$; (b) $12 \mu\text{m} \times 4 \mu\text{m}$; (c) $6 \mu\text{m} \times 2 \mu\text{m}$. Sources are denoted by a gray o, while the + and – symbols denote signed dislocations using the sign convention of Fig. 2.

4. Conclusions

The dislocation structures that develop during bending, both with a single slip system and with multiple slip systems, involve arrays of dislocations that give rise to a rotation consistent with the imposed rotation. These are the geometrically necessary dislocations of Nye (1953) and Ashby (1970). For the micron-size strips considered, there is a dislocation-free region at the lateral free surfaces. When account is taken of this region, the computed dislocation densities in single slip are in very good agreement with what would be expected from simple considerations of geometric necessity. In addition, when there are multiple slip systems available, a considerable fraction of the dislocations are statistical. These statistical dislocations affect the evolution of the hardening. Because the dislocation structures that develop are very different from what occurs in the same specimen subject to plane strain tension, there is no simple relation between the tensile stress–strain response and the bending moment–rotation response. There is a distinct size effect in bending that is mainly associated with the geometrically necessary dislocations.

The deformation mode in bending involves slip along slip bands that are oblique to the elastic neutral axis. Slip tends to concentrate on a fraction of all potential slip planes, leaving distinct slip traces on the deformed specimen. This pattern is quite consistent with that shown by Nadai (1950) for multiple slip and by Gilman (1955) for single slip.

The present simulations show that the mean spacing between these slip bands is to a large extent set by the geometrically necessary dislocations. The initial locations where dislocation activity starts are statistically determined by the distribution of dislocation sources with different strengths, but as plasticity spreads out through the specimen, distinct slip bands form at spacings that scale with the height of the bent strip. The mean spacing for a given specimen will of course decrease with continued bending as the dislocation density grows. Thus, bending shows that the slip band spacing is not controlled only by material length scales, i.e. the Burgers vector, but also by the dislocation structures that are determined by the state of deformation.

The deformation mode in our discrete dislocation calculations is quite different from what a conventional continuum plasticity theory would predict, even if a continuum slip theory were employed to account for the discreteness of slip systems. For a conventional plasticity theory to give rise to highly localized deformations in bending the material response would need to be such that the governing equations lose ellipticity. Such an analysis of bending, but at large strains, that gives rise to deformation patterns similar to Fig. 6(c) is carried out in Triantafyllidis et al. (1982). However, in a conventional continuum plasticity theory, loss of ellipticity implies ill-posed boundary value problems and, in numerical solutions, an inherent dependence of the results on the discretization. Nonlocal continuum plasticity theories (e.g. Walgraef and Aifantis, 1985; Fleck and Hutchinson, 1997; Acharya and Bassani, 1998) hold the promise of giving well-posed solutions. Whether any of these theories gives rise to the deformation mode in bending obtained in the calculations here, and seen in experiments, remains to be seen.

The analyses here indicate that the inelastic bending response of a micron-size specimen or component made of a crystalline solid is substantially different from

that of a more macroscopic structural member. Since the response in bending is often a key design consideration, there may be significant implications for the design of small scale machine elements.

Acknowledgements

The work of H.H.M. Cleveringa is part of the research program of the “Stichting voor Fundamenteel Onderzoek der Materie (FOM)” which is supported financially by the Nederlandse Organisatie voor Wetenschappelijk Onderzoek (NWO). A. Needleman and E. Van der Giessen acknowledge support from the Materials Research Science and Engineering Center on On Micro- and Nano-Mechanics of Materials at Brown University (NSF Grant DMR-9632524).

References

- Acharya, A. Bassani, J.L., 1998. Incompatibility and crystal plasticity, *J. Mech. Phys. Solids* (submitted).
- Amodeo, R.J., Ghoniem, N.M., 1990. Dislocation dynamics I: a proposed methodology for deformation micromechanics. *Phys. Rev.* 41, 6958–6967.
- Ashby, M.F., 1970. The deformation of plastically non-homogeneous materials. *Phil. Mag.* 21, 399–424.
- Besseling, J.F., 1965. In: Przemieniecki, J.S. et al. (Eds.), *Matrix Methods in Structural Mechanics*. US Air Force, Dayton, OH, p. 655.
- Bréchet, Y., Canova, G., Kubin, L.P., 1996. Strain softening, slip localization and propagation: from simulations to continuum modeling. *Acta Mater.* 44, 4261–4271.
- Cleveringa, H.H.M., Van der Giessen, E., Needleman, A., 1997. Comparison of discrete dislocation and continuum plasticity predictions for a composite material. *Acta Mat.* 45, 3163–3179.
- Eshelby, J.D., 1962. The distortion and electrification of plates and rods by dislocations. *Phys. Stat. Sol.* 2, 1021–1028.
- Evans, J.T., 1995. Bending produced by dislocations in a beam. *Int. J. Engng. Sci.* 33, 1321–1329.
- Fang, X.C., Dahl, W., 1993. Investigation of the formation of dislocation cell structures and the strain hardening of metals by computer simulation. *Mater. Sci. Engin.* A164, 300–305.
- Fivel, M.C., Gosling, T.J., Canova, G.R., 1996. Implementing image stresses in a 3D dislocation simulation. *Model. Simul. Mater. Sci. Eng.* 4, 581–596.
- Fleck, N.A., Hutchinson, J.W., 1997. Strain gradient plasticity. *Adv. Appl. Mech.* 33, 295–361.
- Gilman, J.J., 1955. Structure and polygonization of bent zinc monocrystals. *Acta Metall.* 3, 277–288.
- Groma, I., Pawley, G.S., 1993. Role of the secondary slip system in a computer simulation model of the plastic behavior of single crystals. *Mater. Sci. Engin.* A164, 306–311.
- Hirth, J.P., Lothe, J., 1968. *Theory of Dislocations*, McGraw Hill, New York.
- Kubin, L.P., Canova, G., Condat, M., Devincre, E., Pontikis, V., Bréchet, Y., 1992. In: Martin, G., Kubin, L.P. (Eds.), *Nonlinear Phenomena in Materials Science II*. Sci-Tech, Vaduz, p. 455.
- Lubarda, V., Blume, J., Needleman, A., 1993. An analysis of equilibrium dislocation distributions. *Acta Metall. Mat.* 41, 625–642.
- Nabarro, F.R.N., 1967. *Theory of Crystal Dislocations*, Oxford University, Press, Oxford.
- Nadai, A., 1950. *Theory of Flow and Fracture of Solids*, Vol. 1, 2nd Edition. McGraw Hill, New York, p. 367.
- Nye, J.F., 1953. Some geometrical relations in dislocated crystals. *Acta. Metall.* 1, 153–162.
- Pearce, D., Asaro, R.J., Needleman, A., 1983. Material rate dependence and localized deformation in crystalline solids. *Acta Metall.* 31, 1951–1976.
- Polonsky, I.A., Keer, L.M., 1996. Simulation of microscopic elastic-plastic contacts by using discrete dislocations. *Proc. R. Soc. Lond.* A452, 2173–2194.

- Rodin, G.J., 1998. Towards rapid evaluation of the elastic interactions among three-dimensional dislocations. *Phil. Mag. Letters* 77, 187–190.
- Siems, R., Delavignette, P., Amelinckx, S., 1962. The buckling of a thin plate due to the pressure of an edge dislocation. *Phys. Stat. Sol.* 2, 421–438.
- Triantafyllidis, N., Needleman, A., Tvergaard, V., 1982. On the development of shear bands in pure bending. *Int. J. Solids Struct.* 18, 121–138.
- Van der Giessen, E., Needleman, A., 1995. Discrete dislocation plasticity: a simple planar model. *Model. Simul. Mater. Sci. Eng.* 3, 689–735.
- Walgraef, D., Aifantis, E.C., 1985. Dislocation patterning in fatigued metals as a result of dynamical instabilities. *J. Appl. Phys.* 58, 688–691.
- Wang, H.Y., LeSar, R., 1995. $\mathcal{O}(N)$ algorithm for dislocation dynamics. *Phil. Mag.* A71, 149–164.
- Zacharopoulos, N., Srolovitz, D.J., LeSar, R., 1997. Dynamic simulation of dislocation microstructures in mode III cracking. *Acta Mat* 45, 3745–3763.
- Zbib, H.M., Rhee, M., Hirth, J.P., 1998. On plastic deformation and the dynamics of 3D dislocations. *Int. J. Mech. Sci.* 40, 113–127.